High Temperature Corrosion of Materials (2025) 102:27
https://doi.org/10.1007/s11085-025-10344-4

RESEARCH

Effect of the Different Alloying Elements Mo, Ti and Si in Aluminized Mo-Based Silicides

Katharina Beck[1] · Till König[1] · Ceyhun Oskay[1] · Andreas K. Czerny[2] · Frauke Hinrichs[3] · Georg Winkens[3] · Anke S. Ulrich[4] · Martin Heilmaier[3] · Mathias C. Galetz[1]

Received: 19 August 2024 / Revised: 25 June 2025 / Accepted: 27 June 2025 /
Published online: 8 August 2025

Abstract

To understand the influence of Mo, Si, and Ti during aluminizing pack cementation processes of Mo-Si-Ti alloys, two ternary Mo-Si-Ti alloys (eutectic Mo-20.0Si-52.8Ti and eutectoid Mo-21.0Si-34.0Ti) were investigated and compared with pure Ti and Mo-40Ti (all in at.%). The coating formation mechanisms, phase composition, and microstructures of the different substrates were compared. Subsequently, the effect of the different elements on the oxidation behavior was evaluated, using thermogravimetric analysis at 700 °C and 900 °C for 100 h in synthetic air. In addition, the type I (900 °C) and type II (700 °C) hot corrosion behavior of the Al-coated Mo-Si-Ti alloys was investigated for 24 h and 100 h in synthetic air + 0.1% SO_2. While the initial Al-rich coating phase was consumed or transformed at 700 °C, it successfully facilitated the formation of a protective Al_2O_3 scale on the surface, even if the underlying reservoir was diminished. At 900 °C, the Al coatings on both substrates failed, and a hot corrosion-induced pesting dominated. While Si generally has a positive effect on oxidation and hot corrosion resistance, the main impact of Mo is dictated by its evaporation, and Ti can lead to the formation of TiO_2 as a mixed oxide with Al_2O_3.

Keywords Aluminum coating · High-temperature applications · Hot corrosion · Oxidation resistance · Pack cementation · Silicides

Introduction

Due to their high melting points around 2000 °C, refractory metal-silicide alloys are promising alternatives to Ni-based superalloys as structural materials in high-temperature processes [1]. In recent years, Mo-Si-Ti alloys have been of particular interest because of their high creep strength in the range similar to single crystal Ni-based alloys [2, 3] and their oxidation resistance up to 1300 °C [2–4]. The ternary

Extended author information available on the last page of the article

alloy compositions in the Mo-Si-Ti system were synthesized forming fine lamellar microstructures by either a eutectic reaction (L → (Mo,Ti,Si) + $(Ti,Mo)_5Si_3$; Mo-20.0Si-52.8Ti) or a eutectoid reaction ($(Mo,Ti)_3Si$ → (Mo,Ti,Si) + $(Mo,Ti)_5Si_3$; Mo-21.0Si-34.0Ti) [5, 6]. The eutectic alloy exhibited pesting resistance in the intermediate temperature range (700 °C to 900 °C), while the eutectoid alloy suffered catastrophic mass losses [4, 5]. The various influencing factors on the oxidation behavior of these two compositions, such as chemical composition, phase fraction, and lateral scale thickness, can be found in the literature [7].

Despite the promising results regarding the eutectic Mo-Si-Ti alloy, the sensitivity of the oxidation resistance to small compositional and microstructural changes, especially in the pesting regime, requires a more robust solution. Pack aluminization has been proven to be an effective tool to increase the oxidation resistance of Mo, Mo-alloys [8–12], and Ti alloys [13–16]. Al, as a coating element, offers several advantages over other potential elements or combinations thereof, such as Si [17, 18], Si-B [19–22], or Cr [4], because the formation of intermetallics in the subsurface zone causes a reduction in Gibbs energy, and thus a strong driving force for coating formation. Aluminides potentially form dense, slow-growing α-alumina scales, which are preferred in most high-temperature applications, over a wide range of temperatures, including the pesting range. At the same time, it is necessary to understand the impact of the alloying elements in the substrate material on coating formation and oxidation.

Besides the conventional dry oxidation behavior, the resistance against hot corrosion, a common phenomenon in turbines, needs to be investigated [23]. Na_2SO_4 is considered the main cause of hot corrosion and arises during combustion when traces of Na and S are present in the engine from fuel or air impurities [24–26]. Type I hot corrosion of Ni-based alloys occurs between 800 °C and 950 °C, and is caused by liquid Na_2SO_4 deposits, which results in a uniform attack of the material [27–29]. Type II hot corrosion takes place below the melting point of Na_2SO_4 in the temperature range 650–800 °C [30, 31]. Eutectic mixtures of Na_2SO_4 with other sulfate salts (typically $NiSO_4$ or $CoSO_4$) leads to the formation of liquid deposits, causing a localized attack of the metallic material (pitting) [27, 28]. While the hot corrosion behavior of Ni-based alloys is well understood, information on potential refractory metal-based alternatives is still scarce in the literature.

In this study, Al diffusion coatings are applied on two different Mo-Si-Ti alloys (eutectic Mo-20.0Si-52.8Ti and eutectoid Mo-21.0Si-34.0Ti) to form mainly Al_3Ti on the surface. The coatings' performance is compared to that of aluminized Ti, which forms pure Al_3Ti and thus can be used as a baseline to determine the influence of the different alloying elements on the oxidation of the Al_3Ti phase. Aluminized Mo-40Ti was selected to mimic a Si-free material with a high Mo/Ti ratio. The isothermal oxidation behavior of the four different systems is examined, focusing on the pesting regime of Mo-based alloys between 700 °C and 900 °C. Since the Al-coated Mo-Si-Ti alloys demonstrated the best oxidation resistance, their type I (900 °C) and type II (700 °C) hot corrosion behavior under a Na_2SO_4 deposit is also investigated.

Experimental Procedures

Alloy Manufacturing

Three Mo-based alloy compositions (Mo-40Ti, eutectic Mo-20.0Si-52.8Ti, and eutectoid Mo-21.0Si-34.0Ti (all in at.%)) and pure Ti (≥ 99.60%, Goodfellow) were chosen as substrates. The alloys were prepared in an arc melter (AM/0.5, Edmund Bühler GmbH) from elemental materials Mo (99.95%, EVOCHEM), Si (99.99%, ChemPUR) and Ti (≥ 99.8%, ChemPUR).

After evacuating the vacuum chamber to 10^{-4} mbar, the arc melting process was performed at an Ar (> 99.998%) base pressure of 600 mbar on a water-cooled Cu crucible. The ingot was repeatedly melted five times and flipped after each step to ensure a homogeneous alloy composition. A Zr getter was remelted before each melting step to keep the residual oxygen in the vacuum chamber as low as possible. In an additional arc melting step, rods of 12–14 mm in diameter and a typical length of 150 mm were produced through drop casting of the Mo-Si-Ti ingots into a water-cooled Cu mold. Subsequently the Mo-21.0Si-34.0Ti alloy was heat treated at 1300 °C for 200 h under Ar (> 99.998%) atmosphere in a resistance tube furnace (HTRH 70-600/18, Carbolite Gero GmbH & Co. KG). All samples were cut, using arc wire cutting, to the required geometries (Mo-Si-Ti alloys: height of 3 mm and 12–14 mm in diameter; Ti and Mo-40Ti alloy: 10 mm × 10 mm × 3 mm) and grinded with P 500 SiC paper to remove any Cu contamination that could have been introduced by wire erosion. Finally, the surface was cleaned in acetone in an ultrasonic bath to remove any remaining organic impurities.

Coating Manufacturing

The powder compositions and temperatures used during the pack cementation processes [32] are summarized in Table 1. The pack cementation powders for producing the Al diffusion coatings included Al (≥ 99.5%, grain size ≤ 160 µm, Roth), a halide activator (NH_4Cl, ≥ 99.5%, grain size ≤ 1.3 mm, Honeywell), and Al_2O_3 as an inert filler (≥ 98%, grain size ≤ 130 µm, Honeywell).

The individual alloys were coated as a set of four in a covered alumina crucible with an average powder-to-surface area ratio of 6–8 g cm^{-2}. Following a 6 h drying period at 150 °C, the pack cementation was carried out in a quartz tube furnace (HZS 12/600, Carbolite Gero GmbH & Co. KG). After the coating temperature was

Table 1 Pack cementation conditions for the different substrate materials

Substrate	Powder composition	Temperature	Atmosphere
Ti	5 wt.% Al, 0.5 wt.% NH_4Cl	800 °C	Ar
Mo-40Ti	1 wt.% Al, 1 wt.% NH_4Cl	1000 °C	Ar
Mo-20.0Si-52.8Ti	1 wt.% Al, 1 wt.% NH_4Cl	1000 °C	Ar
Mo-21.0Si-34.0Ti	1 wt.% Al, 1 wt.% NH_4Cl	1000 °C	Ar

Ti was pack cemented at a lower temperature than the other substrates due to its allotropic transformation at 882 °C [33]

reached at a rate of 7 °C min^{-1}, it was maintained for 8 h under an Ar atmosphere (99.999%, Air Liquide) with a flow rate of approximately 102 cm h^{-1}. Pack cementation processes are often performed in inert atmospheres (e.g., Ar with 5 vol.% H_2 added) to prevent the oxidation of the materials. In this study, pure Ar is used, as H_2 led to pronounced crack formation on the Ti-rich substrates. This is attributed to the susceptibility of Ti to hydride formation and hydrogen embrittlement [34–36]. After the pack cementation, the samples were cleaned in acetone in an ultrasonic bath for 10 min.

Oxidation

Thermogravimetric analysis (TGA) was used to investigate the oxidation kinetics of the Al-coated substrates. The samples were oxidized at 700 °C (M25D-V, Sartorius; RAS 50/250/12, Thermconcept) and 900 °C (TGA 92, Setaram; TZF 12/65/550, Carbolite Gero GmbH & Co. KG) in dry synthetic air (80% N_2 and 20% O_2 with a flow rate of approx. 205 cm h^{-1}) while the mass change as a function of time was recorded up to 100 h. The samples were placed in a holder made from quartz glass, which was attached to the precision balance. The furnace was heated at a rate of 10 °C min^{-1} until the oxidation temperature was reached. After the experiment, the furnace was turned off, and the samples remained inside while the furnace cooled down.

Hot Corrosion

By evaporating a saturated Na_2SO_4 solution, a salt deposit of 2.5 mg cm^{-2} was deposited on the preheated (~100 °C) Mo-Si-Ti alloys. Subsequently, the salt-coated samples were exposed to the hot corrosion environment, dry synthetic air (99.999%, Air Liquide) + 0.1% SO_2 (99.98%, Air Liquide) with a flow rate of approx. 53 cm h^{-1}, at 700 °C and 900 °C. The samples were placed in individual alumina crucibles inside a quartz tube furnace (VST 12/900, Carbolite Gero GmbH & Co. KG). The gas mixture was passed through a Fe_2O_3 catalyst at the beginning of the tube furnace to establish the sluggish chemical equilibrium between SO_2 and SO_3:

$$SO_2 + \frac{1}{2}O_2 \rightleftharpoons SO_3 \tag{1}$$

According to thermodynamic calculations [37], the p_{SO_3} of synthetic air + 0.1% SO_2 atmosphere equals 5.3×10^{-4} atm at 700 °C and 1.3×10^{-4} atm at 900 °C. A drying period of 12 h at 150 °C under pure synthetic air removed residual moisture to prevent the formation of sulfuric acid. Afterward, the hot corrosion temperature was reached at a heating rate of 10 °C min^{-1}. After the experiment, the furnace was turned off. The samples remained inside while the furnace cooled down under pure synthetic air.

Analysis

Using the Leica MZ16 A stereomicroscope, macroscopic images of the samples were taken before and after pack cementation and after oxidation. X-ray diffraction (XRD) measurements (Bruker D8 Advance A25 equipped with a Cu tube) were used to analyze the phases formed during pack cementation and oxidation. A Renishaw inVia Raman spectroscope was used to further characterize the thin oxide films ($\lambda = 633$ nm). Cross sections of the samples were prepared using metallographic methods, including Ni-electroplating, mounting in epoxy, wet automated grinding (to P 2400), and polishing with 3 µm and 1 µm diamond suspensions and a colloidal silicon oxide suspension. Light microscopy and scanning electron microscopy (SEM, Hitachi FlexSEM 1000II with an energy-dispersive X-ray spectrometer (EDS)) were utilized to examine the cross sections, to determine the thicknesses of the layers, and standard deviations by averaging four or more separate measurements. The JOEL JXA-8100 electron probe microanalyzer (EPMA), equipped with five wavelength dispersive detectors (WDS), was used to conduct quantitative concentration profile measurements (step size of 0.5 µm) and semi-quantitative element mapping.

Results and Discussion

Aluminum Diffusion Coatings

Figure 1 shows cross-sectional BSE images after pack cementation of Ti, Mo-40Ti, and both Mo-Si-Ti alloys. On Ti and Mo-40Ti an Al_3Ti phase (tetragonal, *I*4/*mmm*, 139) formed on the surface (see Fig. 10), as previously reported in the literature for Ti-based alloys [38–40]. The Al content close to the surface of Mo-40Ti was between 72–73 at.%, corresponding to the $D8_8$ phase of Al_3Ti, which is stable above 977 °C in the binary Al-Ti system [41]. On pure Ti, the Al content was similar at 71 at.%, although at 800 °C the Al_3Ti phase should allow a higher Al content [41]. Below the Al_3Ti layer, intermetallic phases with lower Al contents were present in the interdiffusion zone, which were too thin at this stage to be characterized in detail. After exposure at 700 °C they grew and could be identified as Al_2Ti and $AlTi_3$ (see Fig. 4(a)). Due to the lower pack cementation temperature, the layer deposited on Ti was considerably thinner than on all other substrate materials. On Mo-40Ti, the Al_3Ti layer contained about 15 at.% of dissolved Mo, which is in the range of theoretically and experimentally determined Mo solubilities in Al_3Ti [42]. Closer to the substrate, the Mo-rich Al_8Mo_3 phase precipitated in the Al_3Ti phase, and a (Mo,Ti)Al layer occurred at the interface to the substrate, where the Al content decreased due to interdiffusion (see Fig. 1(b)). According to the phase diagram (see Fig. 2) for a Mo-40Ti alloy enriched with Al, three phases can be expected in equilibrium (Al_3Ti, Al_8Mo_3, and Al_3Mo) [43]. Their distribution in the coating being more Ti-rich at the surface suggests the preferred outward diffusion of Ti over Mo.

By comparing the single phase materials with the coatings formed on the Mo-Si-Ti alloys the higher surface roughness became apparent, even though the

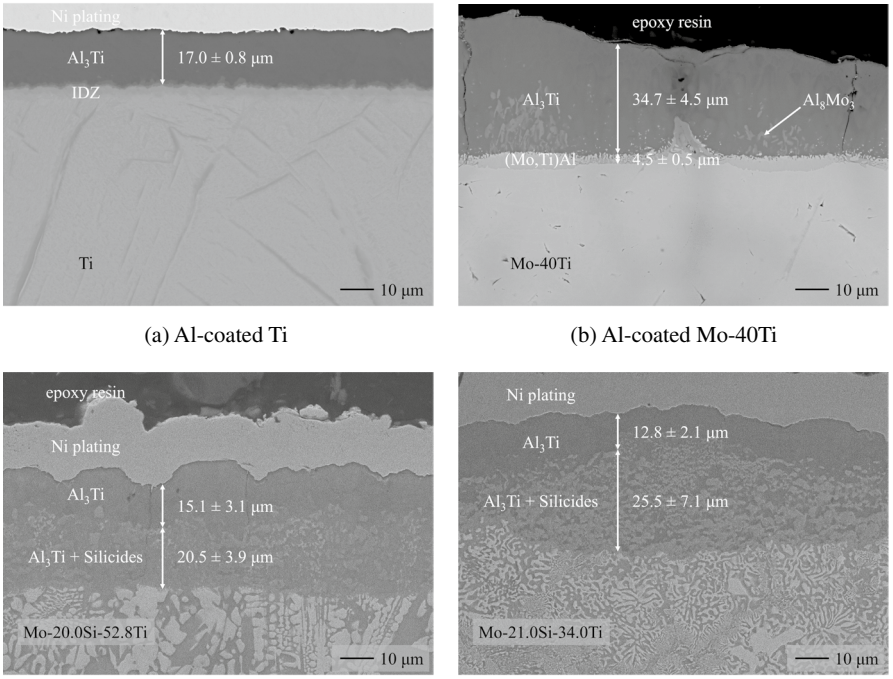

(a) Al-coated Ti

(b) Al-coated Mo-40Ti

(c) Al-coated eutectic Mo-20.0Si-52.8Ti

(d) Al-coated eutectoid Mo-21.0Si-34.0Ti

Fig. 1 BSE images of the coating illustrating the distinct phases formed on the binary Mo-Ti alloy and ternary Mo-Si-Ti alloys after Al pack cementation

surface finish of all samples before pack-cementation was the same. An Al_3Ti phase formed on the surface of both Mo-Si-Ti alloys, but the amount of dissolved Mo was different. Quantitative EPMA measurements revealed that the dissolved Mo content was lower in the Ti-rich eutectic alloy with around 10 at.% in contrast to 15 at.% in the eutectoid alloy; 15 at.% matched the value for the Si-free Mo-40Ti alloy. The measured Mo/Ti ratio was lower than in the Mo solid solution, confirming the preferred outward diffusion of Ti over Mo. The Al content in the outer precipitate-free part of the coating was between 72–73 at.%, corresponding to the maximum Al content in the $D0_{22}$ variant of Al_3Ti, which is stable above 977 °C in the binary Al-Ti system [41, 44, 45]. Quantitative EPMA line scans revealed a maximum Si content of 3.0 at.% in the Al_3Ti phase in both Mo-Si-Ti alloys, which was only slightly above the 2.3 at.% Si found before at 700 °C for an Al-Ti-Si system without Mo [46].

In contrast to Mo-40Ti, no Mo-rich intermetallic phase was found within the coatings deposited on the eutectic and eutectoid Mo-Si-Ti, but closer to the metal interface titanium silicide precipitates were found, reflecting the microstructure of the substrate. EPMA point measurements showed that these matched the $(Ti,Mo)_5Si_3$ with a hexagonal $D8_8$ structure. According to quantitative EPMA line-scans the silicides were enriched with 9–23 at.% Al depending on the position within the coating. However, the lateral resolution limitations of EPMA might lead to an overestimation of the Al content of the small silicide inclusions surrounded by the Al_3Ti

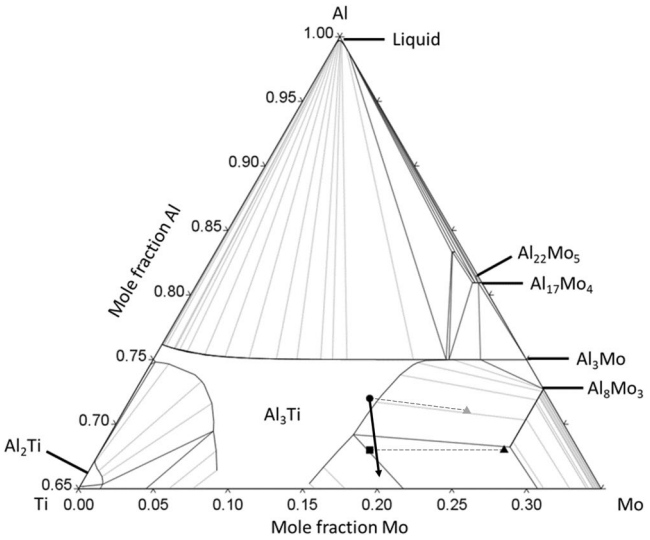

Fig. 2 Isothermal section of the phase diagram of the ternary Al-Mo-Ti system at 900 °C. The dot indicates the composition of the coating after the pack cementation process. The square indicates the composition of the coating after exposure to the oxidizing atmosphere at 900 °C. The triangles indicate the composition of the second Mo-rich phases after exposure (700 °C in light gray and 900 °C in black). The arrow indicates the depletion of Al in the direction of the composition of the substrate during oxidation. The dotted lines indicate which phases are in equilibrium with each other. The phase diagram was calculated (Thermo-Calc) using the dataset published by Distl et al. [47]

phase. In previous studies of the ternary systems Al-Ti-Si and Al-Mo-Si, the comparable phases Ti_5Si_3 and Mo_5Si_3 dissolved up to 6 at.% Al at 700 °C [46] and up to 12.5 at.% at 1400 °C [48], respectively. In a recent reassessment of the Al-Mo-Si system it was suggested that the Al solubility is not particularly dependent on temperature and remains at about 10 at.% at lower temperatures [49]. Hence, it is hypothesized that combining Ti and Mo on the A site of the A_5Si_3 phase might increase the solubility of Al. Additionally, an experimental and thermodynamic investigation of the Mo-Si-Ti system confirmed that Ti and Mo can be substituted over a wide range in Ti_5Si_3 [50]. As expected from the ratio between Ti and Mo in the substrate, the titanium silicides within the eutectic alloy had higher Ti contents and dissolved smaller amounts of Mo, while in the eutectoid alloy lower Ti contents were measured and larger amounts of Mo were found in the precipitates. The higher amount of Mo in the eutectoid alloy was also reflected in small precipitates extremely low in Ti found inside the Al_3Ti phase close to the coating/substrate interface, indicating the Al_8Mo_3 phase, which was found before within the coating on Mo-40Ti.

Multiple features imply the formation of partially outward-grown coatings due to Ti diffusion, such as the Mo/Ti ratio and the precipitate-free (silicides or Al_8Mo_3) outer layers. Similarly, it can be argued that the precipitate-rich layers of Al_3Ti were formed more likely by inward diffusion of Al, forming Al_3Ti, enriching the silicides in Al, and even forming Mo aluminides if the Mo solubility in both phases was exceeded. Based on this mechanism, the influence of Ti, the main coating-forming

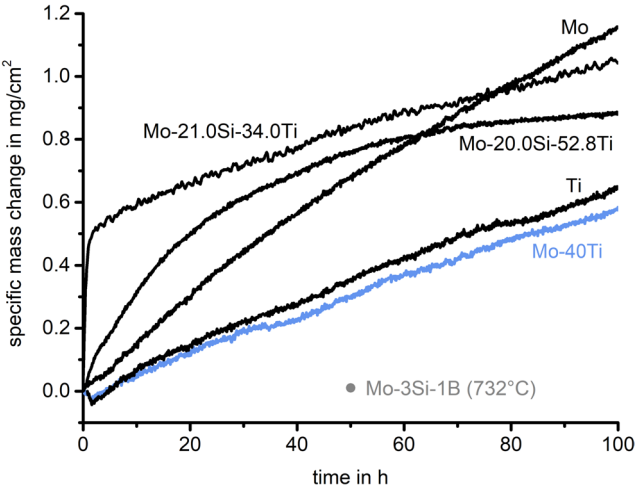

Fig. 3 Overview of the mass gain curves obtained by thermogravimetric analysis (TGA) of Al-coated substrates at 700 °C in synthetic air for 100 h. Al-coated Mo [51] and Al-coated Mo-Si-B [8] from literature are added for comparison

element of the substrate, was expected to be high. However, the Ti-content of all alloys was sufficient to form a single phase Al_3Ti. Only the proportions of precipitate-free to precipitate-rich Al_3Ti were slightly different for the two Mo-Si-Ti alloys. In line with the Ti-content, the precipitate-free layer was thicker on the Ti-richer alloy. By comparing the Mo-40Ti and the Mo-Si-Ti alloys, the influence of Si on the coating formation became apparent: Ti decreases the amount of Mo aluminides because the (Mo-rich) silicides bind the Mo, and no (Mo,Ti)Al layer was observed.

Oxidation Behavior in Synthetic Air

Exposure at 700 °C

Figure 3 displays the mass changes of the Al-coated substrates at 700 °C compared to the literature values of Al-pack cemented Mo [51] and Mo-Si-B [8].

The aluminide coating on pure Mo consisted of an outer Al_8Mo_3 (~ 50 µm) layer and an inner $AlMo_3$ (~ 7 µm) phase [51]. On the Mo-9Si-8B (in at.%) alloy an Al_8Mo_3 matrix (~ 80 µm) with $Mo(Si,Al)_2$ and MoAlB inclusions was deposited [8].

For Al-coated Ti and Mo-40Ti, both with an Al_3Ti phase on the surface, a very similar linear mass gain was observed. The coated Mo-Si-Ti alloys exhibited initially faster kinetics, which were more parabolic and slowed down over time. When comparing Ti, Mo-40Ti, and the two different Mo-Si-Ti alloys, the weight gains of Mo-rich materials were lower without Si, but higher with Si, than their respective counterparts. To understand this, volatile oxides have to be considered. For instance, Al-coated pure Mo [51] produced the highest and mainly linear mass gain, as evaporating MoO_3 creates cavities inside the alumina scale when Al_8Mo_3 is oxidized, allowing for continuous scale growth. The formation of volatile Mo oxides becomes

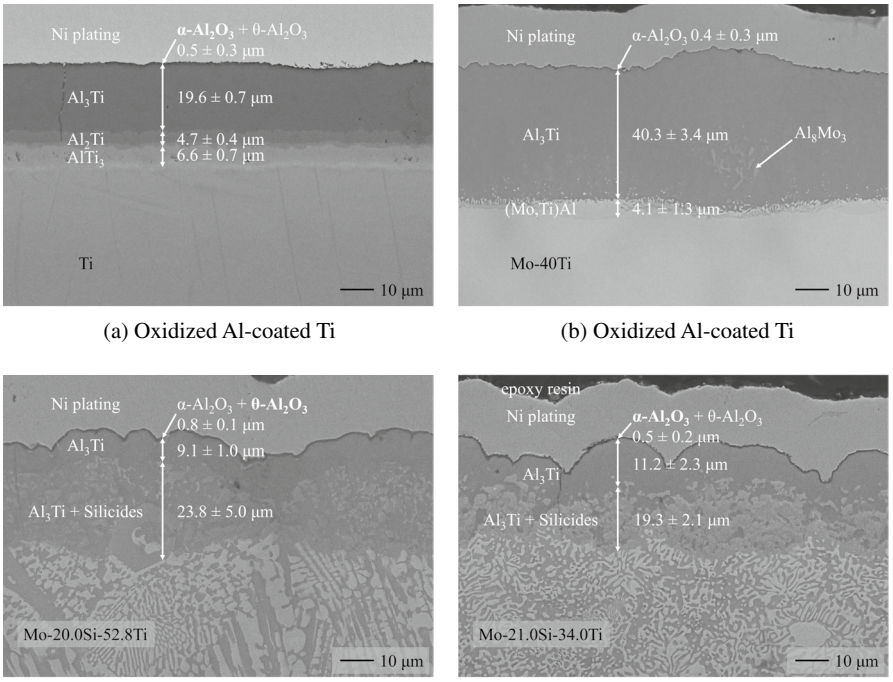

Fig. 4 BSE images of the oxides formed on Al-coated substrates after oxidation for 100 h at 700 °C in synthetic air. The Al_2O_3 polymorphs highlighted in bold in the respective images are the ones that form predominantly on the substrate

dominant in Al-coated Mo-Si-B, resulting in a exceptionally low mass gain compared to the other substrates. These findings indicate that small amounts of B and Si can significantly alter the oxidation behavior of the Al_8Mo_3-based coatings, even as much as Si alone for the Al_3Ti coatings on the Mo-Si-Ti substrates. However, with or without such elements, the results demonstrated that Al_8Mo_3 was generally less protective than the coatings based on Al_3Ti due to the evaporation of Mo oxides. But even for the Al_8Mo_3 phase, it was found that higher Mo contents resulted in faster oxidation kinetics.

Figure 4 displays cross sections of the Al-coated substrates after 100 h at 700 °C. On all samples an Al_2O_3 scale was formed, which was further investigated using Raman and XRD analyses. This is consistent with previous studies, reporting that Al_3Ti is able to form a pure α-Al_2O_3 layer at this temperature [52–55].

Compared to the as-coated state (see Fig. 1(a)), a significant enlargement of the interdiffusion zone can be observed on Ti after only 100 h. Two additional distinct aluminide layers with lower Al content (Al_2Ti and $AlTi_3$) have formed beneath the Al_3Ti layer. In Mo-40Ti, interdiffusion was significantly less pronounced, and Mo-rich precipitates (Al_8Mo_3) were still observed in approximately the same quantity and size within the coatings when compared to the as-coated state (compare

Fig. 1(b)). The composition of the coating in the as-coated state (which only minimally changed during the 700 °C exposure) and the composition of the precipitates are shown in the phase diagram (see Fig. 2).

For both Mo-Si-Ti alloys, no significant interdiffusion was observed, thus the microstructure differed from the as-coated state (see Figs. 1(c) and 1(d)) only by the Al_2O_3 layer formed during oxidation. On the eutectic alloy, mainly θ-Al_2O_3 was formed, which is a commonly present intermediate polymorph during the transition from the low-temperature polymorph γ-Al_2O_3 to the preferred high-temperature polymorph α-Al_2O_3 [56]. Si was previously found to accelerate the outward growth of θ-Al_2O_3 [57] and elevate the γ-Al_2O_3 to α-Al_2O_3 transition temperature [58]. However, after 100 h, on the eutectoid alloy mainly α-Al_2O_3 was formed. Si seems to foster parabolic oxidation behavior compared to the more linear, silicon-free counterparts. On both Mo-Si-Ti alloys the remaining aluminide reservoirs entirely prevented the oxygen uptake and nitridation of the substrate during oxidation at 700 °C, which had been reported before for the uncoated materials [4].

The predicted layer thicknesses calculated from the mass increases and density of Al_2O_3 are considerably higher than the layer thicknesses actually measured. There are various reasons for this divergence: (i) The high surface roughness of the Al-coated Mo-Si-Ti alloys (compare Figs. 1(c) and 1(d)) led to a significantly increased actual surface area. This increase was not considered when determining the surface area used for the plot in Fig. 3. (ii) Due to the edge effects, the oxides formed there are approximately twice as thick as the oxides formed on the surfaces of the samples. (iii) The formation of fast-growing oxides in the early stages of oxidation contributed to higher mass gains. (iv) Additionally, an increased attack was observed at local defects (1–2 per sample), leading to oxide accumulations that were much thicker than the average.

Exposure at 900 °C

Figure 5 illustrates the thermogravimetric measurements of the Al-coated substrates at 900 °C along with the literature data [8, 51]. As already noted at 700 °C, the Al-coated Mo exhibited a linear mass increase in the first few hours of oxidation. At 900 °C, after about 10 h, the aluminide layer failed, followed by catastrophic oxidation. Subsequently, the Mo substrate was converted into volatile MoO_3, explaining the drastic mass loss. While the mass increase of Al-coated Ti was higher than the one at 700 °C, all other Mo-containing alloys had a lower mass gain compared to the oxidation at 700 °C, because of increased MoO_3 evaporation. The course of the Al-coated Mo-40Ti curve showed an increase in weight gain after about 40 h, suggesting lower evaporation after a certain time.

Figures 6 and 7 display cross sections of the Al-coated substrates after 100 h of oxidation at 900 °C. As the coating-substrate interactions were more pronounced at 900 °C than at 700 °C, semi-quantitative EPMA element distribution maps are added to supplement the BSE images. In addition, the layer thicknesses of the remaining coatings, including interdiffusion zones, are summarized in Table 2.

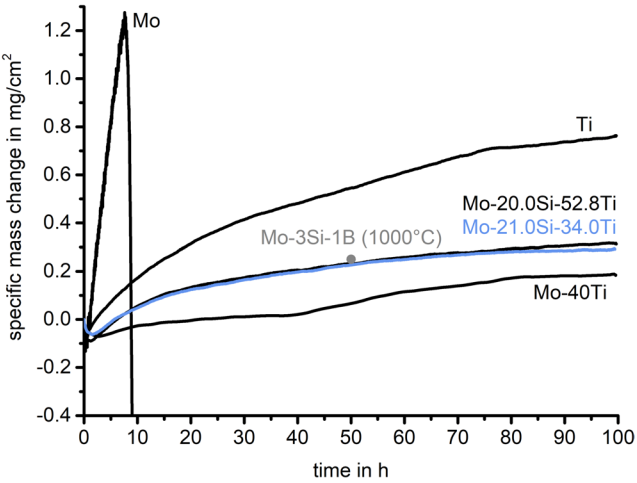

Fig. 5 Overview of the smoothed mass changes measured using TGA of Al-coated substrates at 900 °C in synthetic air for 100 h. Al-coated Mo [51] and Mo-Si-B [8] from the literature are added for comparison

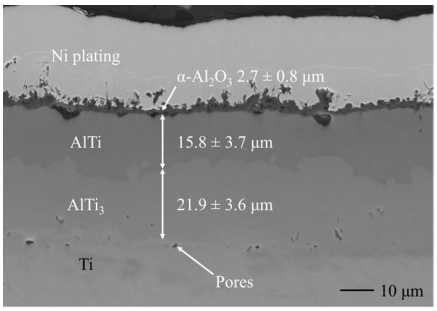

(a) Oxidized Al-coated Ti

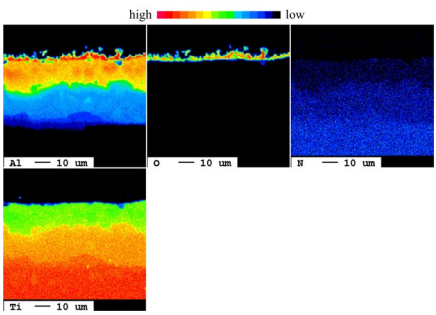

(b) Oxidized Al-coated Ti

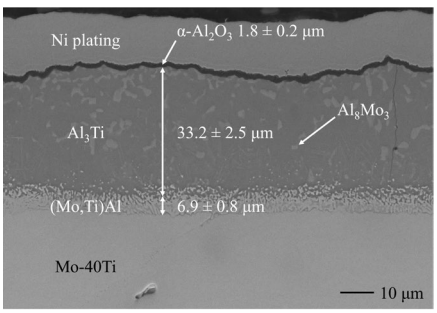

(c) Oxidized Al-coated Mo-40Ti

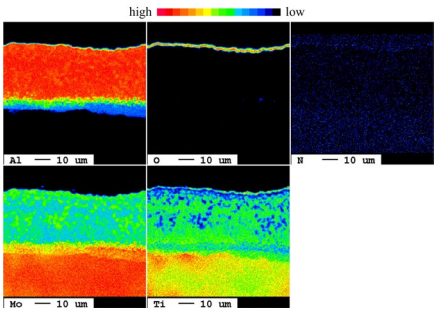

(d) Oxidized Al-coated Mo-40Ti

Fig. 6 BSE images and EPMA maps of the oxides formed on Al-coated substrates after oxidation for 100 h at 900 °C in synthetic air

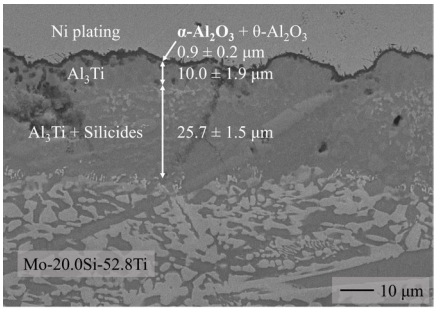

(a) Oxidized Al-coated Mo-20.0Si-52.8Ti

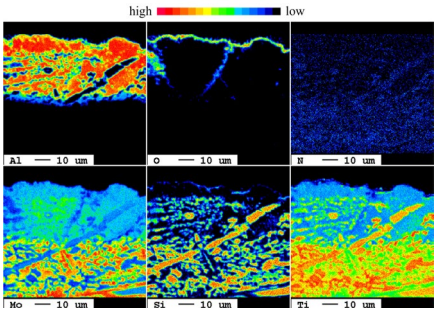

(b) Oxidized Al-coated Mo-20.0Si-52.8Ti

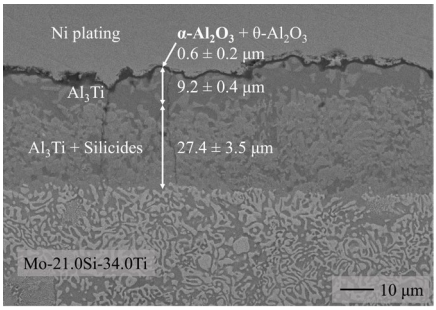

(c) Oxidized Al-coated Mo-21.0Si-34.0Ti

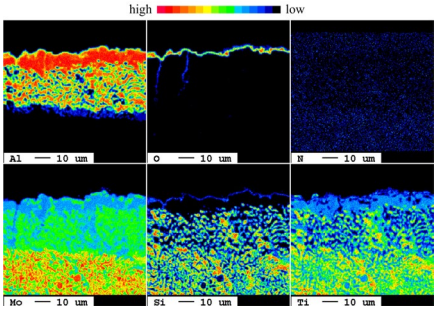

(d) Oxidized Al-coated Mo-20.0Si-34.0Ti

Fig. 7 BSE images and EPMA maps of the oxides formed on Al-coated substrates after oxidation for 100 h at 900 °C in synthetic air. The Al_2O_3 polymorphs highlighted in bold in the respective images are the ones which form predominantly on the substrate

Table 2 Overview of the layer thicknesses of the remaining coatings, including interdiffusion zones, found on the different substrate materials. The percentages given in brackets indicate the change compared to the as-coated state

Substrate	As-coated	700 °C	900 °C
Ti	17.0 µm	30.9 µm (+ 82%)	37.7 µm (+ 122%)
Mo-40Ti	39.2 µm	44.4 µm (+ 13%)	40.1 µm (+ 2%)
Mo-20.0Si-52.8Ti	35.6 µm	32.9 µm (– 8%)	35.7 µm (± 0%)
Mo-21.0Si-34.0Ti	38.3 µm	30.5 µm (– 20%)	36.6 µm (– 4%)

The Al depletion in coated Ti was much more pronounced after 100 h of oxidation at 900 °C (Fig. 6(a)) compared to 700 °C (Fig. 4(a)). Below a protective Al_2O_3 scale with minor amounts of TiO_2 on the surface, the Al-leaner intermetallic phases AlTi and $AlTi_3$ were found. Accordingly, the thickness of the intermetallic layer increased in comparison to the as-coated sample and to the sample exposed at 700 °C (see Table 2). At 900 °C, the transformation into the Ti-richer aluminides by interdiffusion is much faster than the Al depletion at the surface and plays the main role for the coating lifetime. This finding is further supported by the formation of

voids at the oxide/aluminide interface, which can be attributed to volume changes due to the $Al_3Ti \rightarrow AlTi$ phase transformation. Additionally, Kirkendall pores were formed at the aluminide/substrate interface due to Ti outward diffusion into the aluminide layers, similar to the outward diffusion occurring during the pack cementation (best visible in Fig. 1 for the Mo-Si-Ti systems).

On the Al-coated Mo-40Ti, a remaining Al-rich Al_3Ti layer was found below the oxide scale (see Fig. 6(c)) with precipitates of a second Mo-rich phase, containing less Al (compositions of the Mo-rich and Ti-rich phases given in Fig. 2). The coating composition reflects the two-phase region $Al_3Ti + Mo_3Al_8$. Slightly further depletion would lead to Mo_3Al, a phase which was already observed in the IDZ of the as-coated sample. With just a minimal increase in the thickness of the interdiffusion zone at 900 °C (see Table 2), the presence of Mo significantly lowered the interdiffusion, as well as the thickness of the formed Al_2O_3 layer (see values given in Figs. 6(a) and 6(c)). Therefore, the addition of Mo drastically decreased the inwards diffusion of Al compared to the pure Ti substrate, and its evaporation led to higher Al activity, which allowed the formation of a more homogeneous Al_2O_3 layer with fewer TiO_2 inclusions.

Compared to Mo-40Ti (see Fig. 6(c)), an even thinner Al_2O_3 layer with a Si-O-rich sub-scale formed on the surface of both Mo-Si-Ti alloys (see Figs. 7(a) and 7(c)), which showed almost the same weight gain. The development of such sub-scales has already been described in the literature, as has the difficulty of detecting them [59–61]. In this work, the detection was possible using semi-quantitative EPMA element maps (see Si map in Figs. 7(b) and 7(d)). Nevertheless, some differences were identified regarding the underlying Al_3Ti layer. Compared to the Mo-40Ti substrate, the presence of Si slows the inward diffusion of Al into the underlying substrate even more than just Mo. The formation of Al_8Mo_3 does not occur within the eutectic or the eutectoid Mo-Si-Ti alloy, and Al_3Ti remains the sole phase in the outer coating after 100 h.

To sum it up, the coating-substrate interactions at 900 °C were much more pronounced than at 700 °C with Mo and Si significantly reducing the interdiffusion. Additionally, the higher temperature as well as MoO_3 evaporation facilitated the selective oxidation of Al. Less Ti in the alloys minimized the influence of TiO_2 on the growth rate, while a silica sub-scale slowed it down.

Oxidation Kinetics

The description of the oxidation kinetics (illustrated in Figs. 3 and 5) is not straightforward when considering mass losses due to MoO_3 evaporation (very obvious e.g., in the initial weight loss of Al-coated Mo-Si-Ti) and superimposed linear and parabolic weight gain terms. Therefore, the TGA curves were fitted using a power function (see Equation 2). The initial mass losses were omitted, and the fit was limited to the remaining curve.

$$y = m \cdot x^{1/b} \tag{2}$$

The values obtained for the oxidation constant b (see Table 3) are close to 1 for Al-coated Ti and Mo-40Ti at 700 °C, confirming the linear oxide growth. For both

substrates, particularly low values of the factor *m* were obtained, which reflects the acceleration of the oxidation reaction. The marginally higher final mass gain of Ti compared to Mo-40Ti aligns with the slightly higher value for *m*. Additionally, the similar mass gains confirm that the evaporation of Mo oxides only marginally influence the linear oxidation kinetics of Al-coated Mo-40Ti at this temperature. Instead, the formation of Ti-rich oxides has a higher influence on the oxidation kinetics. From the oxidation behavior of titanium aluminides [53, 62] it is known that the thermodynamic stabilities of Al_2O_3 and TiO_2 are so close to each other that the competitive growth of these two oxides often prevents the formation of a protective scale with a parabolic growth rate for the stoichiometric composition. Additionally, TiO_2 exhibits high oxygen diffusivity at elevated temperatures [63]. Compared to the lower temperature, an almost two-fold increase of the parameter *b* and a four-fold increase of the factor *m* was observed for the coated Ti at 900 °C, indicating a change from linear oxidation kinetics to parabolic growth. This aligns with the oxidation behavior of Al_3Ti described in the literature [52, 53, 64]. Due to the higher temperature, the slight difference in the oxide stability between Al and Ti is enough to promote the diffusion and selective oxidation of Al_2O_3 (see Fig. 11). The factor *b* for Mo-40Ti at 900 °C was still between linear and parabolic, indicating the contribution of linear kinetics. In accordance with the lower temperature, the value for *m* remained constant. However, Mo-40Ti showed the lowest mass gain, which confirms that the 15 at.% Mo that dissolve from the substrate into the deposited Al_3Ti phase significantly evaporates at 900 °C.

Table 3 Overview of the factors b and m which was determined using a fit of the TGA curves. *Due to a change in the oxidation kinetic after 40 h of exposure, only the part of the curve between 40 h and 100 h was included in the fit. Additionally, the mass change curves of the Al-coated Mo-Si-Ti alloys were fitted assuming paralinear kinetics (Equation 3). The values for parabolic oxidation constant k_p and linear volatilization rate k_v are listed in the table, too

Substrate (Temperature)	Factor b	Factor m	Chi squared
Ti (700 °C)	1.26	0.02	$8.41 \cdot 10^{-5}$
Mo-40Ti (700 °C)	1.16	0.01	$6.81 \cdot 10^{-5}$
Mo-20.0Si-52.8Ti (700 °C)	2.43	0.14	0.00181
Mo-21.0Si-34.0Ti (700 °C)	4.20	0.34	0.00108
Ti (900 °C)	1.90	0.08	$4.17 \cdot 10^{-4}$
Mo-40Ti (900 °C)*	1.53	0.01	$7.42 \cdot 10^{-5}$
Mo-20.0Si-52.8Ti (900 °C)	2.50	0.07	$1.75 \cdot 10^{-4}$
Mo-21.0Si-34.0Ti (900 °C)	2.31	0.05	$2.10 \cdot 10^{-4}$
Substrate (Temperature)	k_p [$g^2\ cm^{-4}\ s^{-1}$]	k_v [$g^2\ cm^{-4}\ s^{-1}$]	Chi squared
Mo-20.0Si-52.8Ti (700 °C)	$4.69 \cdot 10^{-12}$	$1.05 \cdot 10^{-12}$	0.00109
Mo-21.0Si-34.0Ti (700 °C)	$9.77 \cdot 10^{-12}$	$2.50 \cdot 10^{-12}$	0.00473
Mo-20.0Si-52.8Ti (900 °C)	$1.03 \cdot 10^{-12}$	$4.94 \cdot 10^{-13}$	$8.81 \cdot 10^{-5}$
Mo-21.0Si-34.0Ti (900 °C)	$7.08 \cdot 10^{-13}$	$3.25 \cdot 10^{-13}$	$1.43 \cdot 10^{-4}$

For the two Mo-Si Ti alloys, values above 2 for the factor *b* were obtained, indicating sub-parabolic oxidation kinetics at both temperatures. This illustrates the strong positive influence of Si on oxidation behavior and suggests a contribution of Mo evaporation. The parameter *m* was significantly higher for both materials at 700 °C, indicating a faster acceleration of the oxidation reaction at lower temperatures, which confirmed the influence of Mo evaporation at higher temperatures. As already observed for Ti and Mo-Ti, an increased value for *m* corresponds to a higher final mass increase. The exceptionally high values of both factors for the eutectoid alloy at 700 °C can be explained by the sharp mass increase at the start of the oxidation process. The high initial mass increase is due to the cracks within the coating of the eutectoid alloy, which initially oxidize and close before the surface determines the kinetics. The sub-parabolic oxidation behavior confirms the positive influence of the Si content on the oxidation kinetics of the aluminides investigated. For the Mo-Si-Ti alloys a paralinear fit (Equation 3) of the entire TGA curve was also performed, to better quantify the contributions of oxide layer growth and evaporation.

$$\frac{\Delta m}{A} = \sqrt{k_p \cdot t} - k_v \cdot t \tag{3}$$

This evaporation is high in both systems, but layer growth and the associated mass gain predominates. Interestingly, due to the faster kinetics of oxide growth, the relative contribution of the evaporation is smaller than at 700 °C, even if the absolute amount of evaporated oxides is probably higher.

To sum it up, the kinetic data confirms the microstructural observations such as adding Mo to the substrate material significantly lowers the mass gain rate at 900 °C due to MoO_3 evaporation. Furthermore, higher temperatures facilitate the selective oxidation of Al over Ti, minimizing the influence of TiO_2 (compare Figs. 6(b) and 6(d)), thus enabling the formation of a protective α-Al_2O_3 scale with a parabolic growth rate. With the addition of Si to the substrate, the oxidation kinetics are changed to parabolic or even sub-parabolic at both temperatures. The strong positive influence of Si on the oxidation behavior is evident from the formation of a SiO_2 subsurface scale (best visible in Figs. 7(b) and 7(d)).

Hot Corrosion Behavior

Type I Hot Corrosion

Figure 8 shows cross sections of the Al-coated Mo-Si-Ti substrates after 24 h and 100 h of exposure to type I hot corrosion conditions at 900 °C. On both samples, an outer non-continuous Al_2O_3 layer formed before the oxidation continued in the form of unprotective TiO_2/SiO_2 oxides. After 24 h, the complete Al reservoir was already consumed, which led to a severe corrosion attack. Due to the higher Mo content of the eutectoid alloy and the associated MoO_3 volatilization, the TiO_2/SiO_2 oxide layer formed was significantly thicker compared to the eutectic alloy. After 100 h of exposure there was no metallic material left, and the complete substrate was oxidized.

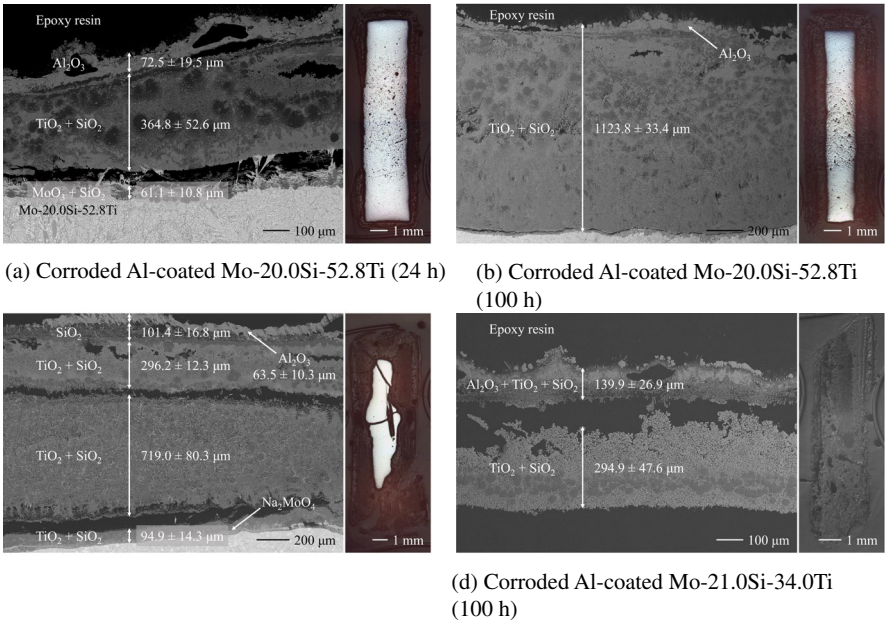

(a) Corroded Al-coated Mo-20.0Si-52.8Ti (24 h)

(b) Corroded Al-coated Mo-20.0Si-52.8Ti (100 h)

(d) Corroded Al-coated Mo-21.0Si-34.0Ti (100 h)

Fig. 8 BSE images of the oxides formed on Al-coated substrates after hot corrosion at 900 °C in synthetic air + 0.1% SO_2. Optical microscopy overview pictures of the cross sections are displayed next to the BSE images

The aluminide coating did not provide sufficient protection against hot corrosion at 900 °C. No protective alumina scale was formed because the Na_2SO_4 deposit significantly reduced the MoO_3 evaporation, as the salt created a local environment where the partial pressure of oxygen is significantly reduced. This decreased the overall formation of Mo oxides and enabled the occurrence of MoO_2, which has a considerably lower partial pressure. Additionally, the deposit caused steric hindrance, further limiting the formation and evaporation of Mo oxides. As a result, MoO_3 volatilization contributed to a notably reduced extent to the local increase of Al activity and accumulation at the sample surface as observed during oxidation. Instead, liquid phases were formed such as sodium molybdate (Na_2MoO_4, melting point 687 °C [65], which arises from the reaction of Na_2SO_4 with MoO_3. A comparison of the partial pressure of MoO_3 ($p_{MoO_3} = 5.21 \cdot 10^{-4}$ bar) and its evaporation from a liquid Na_2MoO_4 deposit ($p_{MoO_3} = 3.15 \cdot 10^{-12}$ bar) likewise demonstrates the reduced oxide volatilization [37]. At both test temperatures, Na_2MoO_4 is known to rapidly dissolve surrounding oxides [66–68], which led to progression of the corrosion. Additionally, the direct reaction of MoO_3 with Al_2O_3 produced aluminum molybdate ($Al_2Mo_3O_{12}$), which was also molten during type I hot corrosion (820 °C (Al_2O_3-rich side) or 740 °C (MoO_3-rich side) [69]). As a result, any protective Al_2O_3 that may have formed at some point cannot be sustained.

Therefore, the hot corrosion behavior was mainly determined by the underlying substrate material and, hence, is similar to the behavior of the uncoated

samples [70] or even worse. After the failure of the pure Al_3Ti layer, the eutectic samples underwent an increased attack as the pack cementation process decreased the Si content at the surface, impeding the formation of a beneficial SiO_2 layer. As known from hot corrosion theory, for a progressive attack, a negative solubility gradient of the oxides involved is required [71, 72], otherwise the liquid phase would eventually become saturated with the dissolved species, and the corrosion attack would stop. After 24 h of exposure (see Fig. 8(a)), characteristic MoO_3 oxide needles [73, 74] were found in the gap at the substrate oxide interface of the eutectic sample. Since it is unlikely that these needle-shaped oxides were formed by solid state diffusion, it is suggested that the MoO_3 needles have reprecipitated from the liquid phase. In addition to reprecipitation, the negative solubility gradient was realized for both Mo-Si-Ti alloys, due to the evaporation of Mo oxides as evidenced by the absence of Mo oxides throughout the oxide scales.

Type II Hot Corrosion

Figure 9 displays cross sections of the Al-coated Mo-Si-Ti substrates next to the corresponding semi-quantitative EPMA element distribution maps after 100 h of exposure to type II hot corrosion conditions at 700 °C. A very similar microstructure was

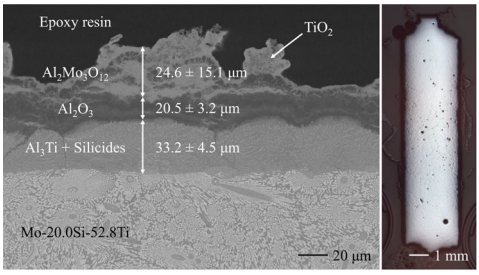

(a) Corroded Al-coated Mo-20.0Si-52.8Ti (100 h)

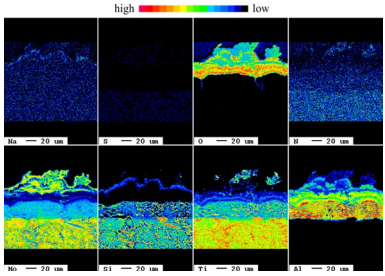

(b) Corroded Al-coated Mo-20.0Si-52.8Ti (100 h)

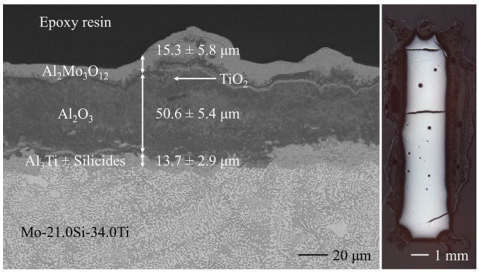

(c) Corroded Al-coated Mo-21.0Si-34.0Ti (100 h)

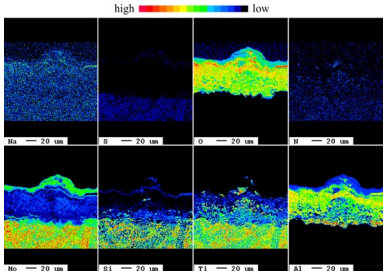

(d) Corroded Al-coated Mo-21.0Si-34.0Ti (100 h)

Fig. 9 BSE images and EPMA maps of the oxides formed on Al-coated substrates after hot corrosion at 700 °C in synthetic air + 0.1% SO_2 (24 h of exposure not shown). Optical microscopy overview pictures of the cross sections are displayed next to the BSE images

found after 24 h of exposure, therefore, these cross sections are not shown here. An extension of the exposure time only led to a thickening of the oxides.

In contrast to 900 °C, the hot corrosion behavior at 700 °C was dominated by the applied aluminide layer, which led to a comparable oxide structure on both samples: $Al_2Mo_3O_{12}$ was found as the outermost oxide layer, with Al_2O_3 underneath and small TiO_2 inclusions throughout the scale. On both samples, remaining aluminides were found beneath the oxides. Due to the higher Mo content in the aluminide layer on the eutectoid Mo-21.0Si-34.0Ti alloy, the remaining Al reservoir was significantly thinner compared to the eutectic Mo-20.0Si-52.8Ti alloy. This can be seen in the macroscopic overview image, in some areas on the eutectoid sample the aluminide layer was consumed, which led to the corrosive attack of the substrate material.

Compared to 900 °C and the hot corrosion behavior of the uncoated substrate materials [70], the aluminide coatings led to a significant improvement in type II hot corrosion resistance. The detrimental Na_2MoO_4, which formed during the exposure of the uncoated alloys [70], was successfully avoided with an Al_2O_3 content of over 20% by the formation of $Al_2Mo_3O_{12}$, becoming the predominant phase [75].

Conclusions

Ti, Mo-40Ti, and two ternary Mo-Si-Ti alloys were aluminized and analyzed to determine the influence of the alloying elements on the coatings' phase formation, morphology, oxidation, and hot corrosion behavior.

- Oxidation experiments at 700 °C and 900 °C revealed a significant influence of the temperature on oxidation kinetics.
- At 700 °C, thin oxides were observed, but only the Si-containing alloys exhibited a parabolic mass gin behavior, while the Ti, Mo-rich, and binary Ti-Mo aluminide coatings grew linear.
- At 900 °C, Mo-oxide evaporation was beneficial and promoted alumina formation. Ti was oxidized alongside Al and accelerated the scale growth, while Si and Mo positively influenced interdiffusion with the substrate.
- While the Al coatings were suitable for oxidative atmospheres at both temperatures, a strong temperature dependence of the protective effect was observed in hot corrosion environments. At 900 °C, the Mo-containing aluminides failed, and led to the formation of liquid phases. At 700 °C, an alumina scale was formed, which protected both Mo-Si-Ti alloys.
- During both oxidation and hot corrosion, the aluminide layers primarily determined the respective behavior, with a secondary dependence on the molybdenum content within these layers.

Appendix A: XRD analysis

See Figs. 10, 11 and 12.

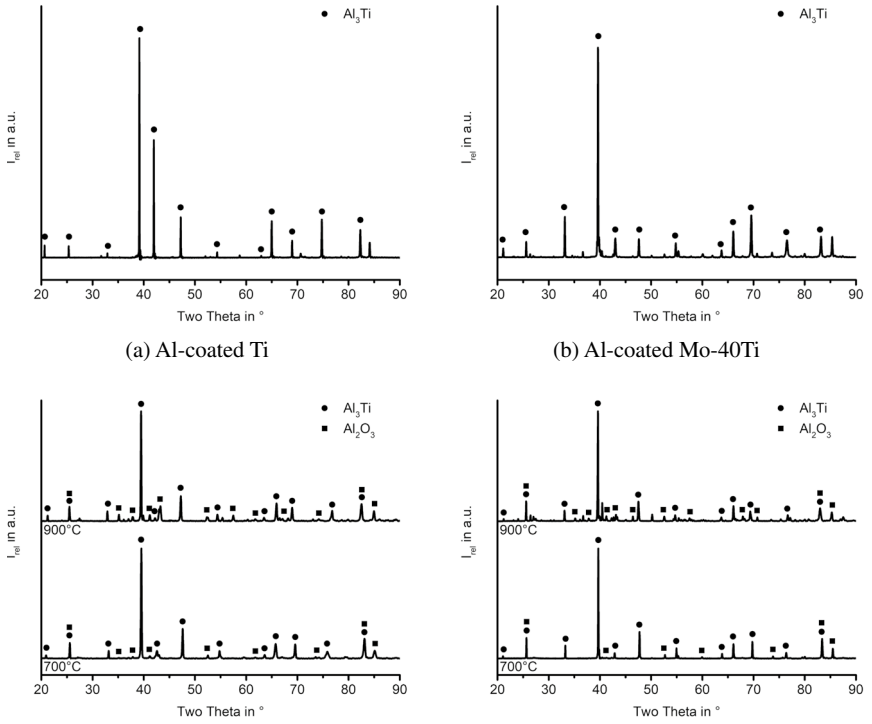

(a) Al-coated Ti

(b) Al-coated Mo-40Ti

(c) Al-coated Mo-20.0Si-52.8Ti

(d) Al-coated Mo-21.0Si-34.0Ti

Fig. 10 XRD diffractograms of the different phases formed on the different substrates after pack cementation

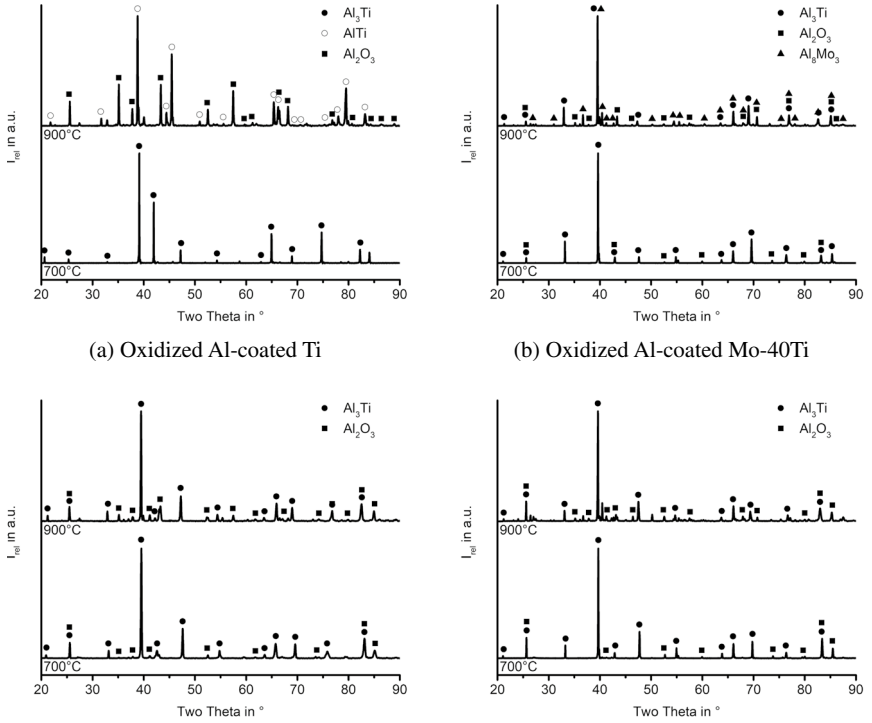

(a) Oxidized Al-coated Ti

(b) Oxidized Al-coated Mo-40Ti

(c) Oxidized Al-coated Mo=20.0Si-52.8Ti

(d) Oxidized Al-coated Mo=21.0Si-34.0Ti

Fig. 11 XRD diffractograms of the oxides formed on the substrates after oxidation

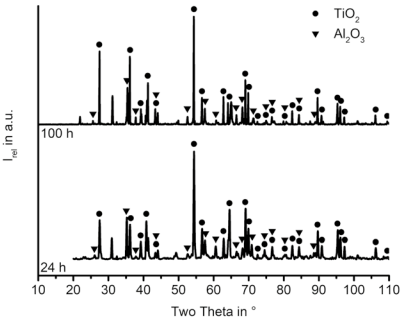

(a) Corroded Al-coated Mo-20.0Si-52.8Ti (900°C)

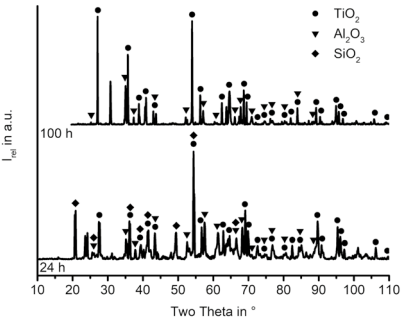

(b) Corroded Al-coated Mo-21.0Si-34.0Ti (900°C)

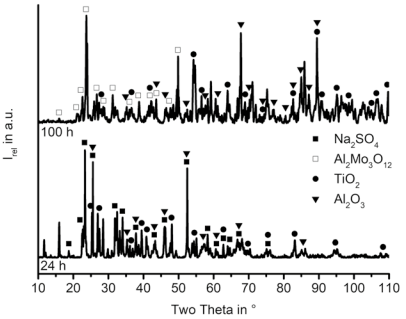

(c) Corroded Al-coated Mo-20.0Si-52.8Ti (700°C)

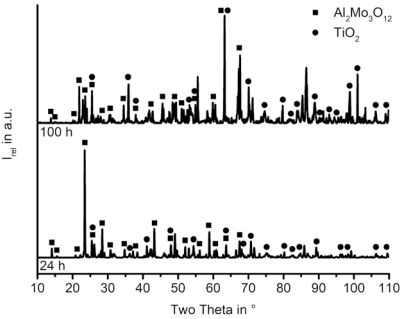

(b) Corroded Al-coated Mo-21.0Si-34.0Ti (700°C)

Fig. 12 XRD diffractograms of the oxides formed on the Mo-Si-Ti substrates after hot corrosion

Appendix B: Raman analysis

See Fig. 13.

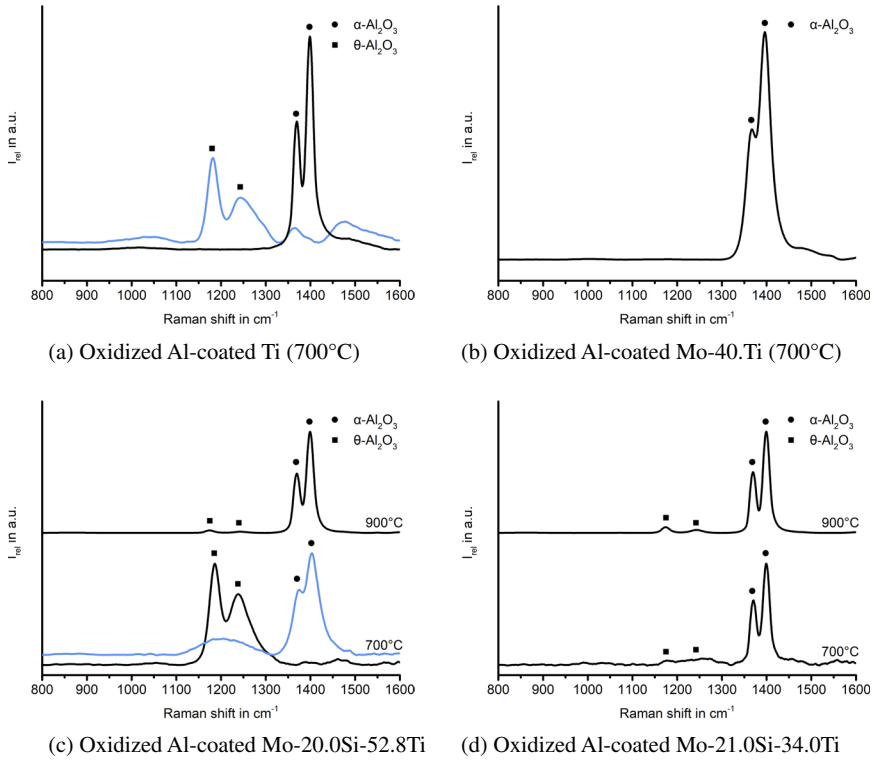

(a) Oxidized Al-coated Ti (700°C)

(b) Oxidized Al-coated Mo-40.Ti (700°C)

(c) Oxidized Al-coated Mo-20.0Si-52.8Ti

(d) Oxidized Al-coated Mo-21.0Si-34.0Ti

Fig. 13 Raman spectra of the oxides formed on the different substrates. The black spectra represent the signals found during the majority of measurements. Sometimes additional signals were found which are shown in light blue

Acknowledgements The authors thank Dr. Gerald Schmidt for EPMA measurements, Mathias Röhrig for technical support, Melanie Thalheimer for SEM support and Susann Rudolphi as well as Daniela Hasenpflug for metallographic preparation.

Author Contributions KB: methodology, investigation, writing—original draft preparation, visualization; TK: writing—review and editing, supervision; CO: writing—review and editing, supervision; AKC: validation, writing—review and editing; FH: resources, writing—review and editing; GW: resources, writing—review and editing; ASU: conceptualization, writing—review and editing, supervision; MH: writing—review and editing, project administration, funding acquisition; MCG: conceptualization, writing—review and editing, supervision, project administration, funding acquisition.

Funding Open Access funding enabled and organized by Projekt DEAL. This work was supported by the Research Training Group 2561 "MatCom-ComMat: Materials Compounds from Composite Materials for Applications in Extreme Conditions" (Project Number: 413956820) funded by the Deutsche Forschungsgemeinschaft (DFG).

Data Availability The data that support the findings of this study are available from the corresponding author upon reasonable request.

Declarations

Conflict of interest The authors declare that they have no conflict of interest.

References

1. J. H. Perepezko, M. Krüger, and M. Heilmaier, *Materials Performance and Characterization* **10**, 2021 (122).
2. S. Obert, A. Kauffmann, and M. Heilmaier, *Acta Materialia* **184**, 2020 (132).
3. S. Obert, A. Kauffmann, R. Pretzler, et al., *Metals* **11**, 2021 (169).
4. K. Beck, F. Hinrichs, C. Oskay, et al., *Coatings* **13**, 2023 (1712).
5. D. Schliephake, A. Kauffmann, X. Cong, et al., *Intermetallics* **104**, 2019 (133).
6. A. Schmitt, K. S. Kumar, A. Kauffmann, et al., *Intermetallics* **90**, 2017 (180).
7. S. Obert, A. Kauffmann, S. Seils, et al., *Journal of Materials Research and Technology* **9**, 2020 (8556).
8. R. Sakidja, F. Rioult, J. Werner, et al., *Scripta Materialia* **55**, 2006 (903).
9. F. Rioult, N. Sekido, R. Sakidja, et al., *Journal of the Electrochemical Society* **154**, 2007 (C692).
10. S. Majumdar, I. Sharma, and A. Suri, *International Journal of Refractory Metals and Hard Materials* **26**, 2008 (549).
11. A. S. Ulrich and M. C. Galetz, *Oxidation of Metals* **86**, 2016 (511).
12. K. Choi, W. Yang, K. H. Baik, et al., *Oxidation of Metals* **92**, 2019 (423).
13. I. Gurrappa, *Oxidation of Metals* **56**, 2001 (73).
14. A. S. Ulrich, N. Laska, A. Straubel, et al., *Materials at High Temperatures* **35**, 2018 (204).
15. N. Chaia, C. Cossu, L. Ferreira, et al., *Corrosion Science* **160**, 2019 (108165).
16. W. Yang, J. Park, K. Choi, et al., *International Journal of Refractory Metals and Hard Materials* **101**, 2021 (105642).
17. K. Ito, H. Numakura, T. Hayashi, et al., *Metallurgical and Materials Transactions A* **36**, 2005 (627).
18. R. Sakidja, J. Park, J. Hamann, et al., *Scripta Materialia* **53**, 2005 (723).
19. Z. Tang, A. J. Thom, M. Kramer, et al., *Intermetallics* **16**, 2008 (1125).
20. J. H. Perepezko and R. Sakidja, *JOM* **62**, 2010 (13).
21. A. Lange, M. Heilmaier, T. A. Sossamann, et al., *Surface and Coatings Technology* **266**, 2015 (57).
22. D. Schliephake, C. Gombola, A. Kauffmann, et al., *Oxidation of Metals* **88**, 2017 (267).
23. G. H. Meier, *Oxidation of Metals* **98**, 2022 (1).
24. P. Hancock, *Corrosion Science* **22**, 1982 (51).
25. V. Lemoine, P. Steinmetz, B. Roques, et al., *Corrosion Science* **25**, 1985 (431).
26. B. Grégoire, X. Montero, M. Galetz, et al., *Corrosion Science* **141**, 2018 (211).
27. R. Bürgel, H. J. Maier, and T. Niendorf, *Handbuch Hochtemperatur-Werkstofftechnik: Grundlagen, Werkstoffbeanspruchungen*, (Springer-Verlag, Hochtemperaturlegierungen und -beschichtungen, 2011).
28. N. Eliaz, G. Shemesh, and R. Latanision, *Engineering Failure Analysis* **9**, 2002 (31).
29. P. Hancock, *Materials Science and Technology* **3**, 1987 (536).
30. J. Stringer, *Materials Science and Technology* **3**, 1987 (482).

31. J. Nicholls, *JOM* **52**, 2000 (28).
32. R. Bianco, M. A. Harper, and R. A. Rapp, *JOM* **43**, 1991 (68).
33. I. Gurrappa, *Journal of Alloys and Compounds* **389**, 2005 (190).
34. C. Briant, Z. Wang, and N. Chollocoop, *Corrosion Science* **44**, 2002 (1875).
35. E. Tal-Gutelmacher and D. Eliezer, *JOM* **57**, 2005 (46).
36. V. Madina and I. Azkarate, *International Journal of Hydrogen Energy* **34**, 2009 (5976).
37. C. Bale, E. Bélisle, P. Chartrand, et al., *Calphad* **54**, 2016 (35).
38. A. Donchev, A. Kolitsch, M. Schütze, et al., *Materials and Corrosion* **62**, 2011 (695).
39. A. Donchev, J. Grüters, M. Galetz, et al., *Advances in Materials and Processing Technologies* **2**, 2016 (471).
40. A. Donchev, M. Galetz, M. Schütze, et al, Protection of Ti-Alloys against high temperature environmental attack by a two step process, aluminization + fluorination. TMS 2014: 143rd Annual Meeting & Exhibition: Annual Meeting Supplemental Proceedings pp 79–85, 2016b.
41. F. Van Loo and G. Rieck, *Acta Metallurgica* **21**, 1973 (61).
42. X. Huang, L. Zhu, G. Cai, et al., *Journal of Materials Science* **52**, 2017 (2270).
43. V. Raghavan, *Journal of Phase Equilibria and Diffusion* **26**, 2005 (357).
44. J. C. Schuster and M. Palm, *Journal of Phase Equilibria and Diffusion* **27**, 2006 (255).
45. H. Wang, R. Reed, J. C. Gebelin, et al., *Calphad* **39**, 2012 (21).
46. Z. Li, C. Liao, Y. Liu, et al., *Journal of Phase Equilibria and Diffusion* **35**, 2014 (564).
47. B. Distl, A. Walnsch, R. F. Mellor, et al., *MSI Eureka* **88**, 2021 (1).
48. P. Eason, K. Jolly, and M. Kaufman, Reassessment of the Mo-Si-Al ternary isotherm at 1400 °C. In: 22nd Annual Conference on Composites, Advanced Ceramics, Materials, and Structures: A: Ceramic Engineering and Science Proceedings, Wiley Online Library, 1988, (437)
49. C. Guo, C. Li, P. J. Masset, et al., *Calphad* **36**, 2012 (100).
50. Y. Yang, Y. Chang, L. Tan, et al., *Materials Science and Engineering: A* **361**, 2003 (281).
51. K. Beck, A. S. Ulrich, A. K. Czerny, et al., *Surface and Coatings Technology* **476**, 2023 130205.
52. J. L. Smialek and D. Humphrey, *Scripta Metallurgica et Materialia* **26**, 1992 (1763).
53. J. Smialek, *Corrosion Science* **35**, 1993 (1199).
54. J.L. Smialek, and N.S. Jacobson, Oxidation of high-temperature aerospace materials. In: High temperature materials and mechanisms. New York: CRC Press 2014, (95–162)
55. J. Grüters and M. Galetz, *Intermetallics* **60**, 2015 (19).
56. S. H. Cai, S. N. Rashkeev, S. T. Pantelides, et al., *Physical Review B* **67**, 2003 (224104).
57. T. L. Barth and E. A. Marquis, *Oxidation of Metals* **95**, 2021 (293).
58. Y. Saito, T. Takei, S. Hayashi, et al., *Journal of the American Ceramic Society* **81**, 1998 (2197).
59. A. S. Ulrich, P. Pfizenmaier, A. Solimani, et al., *Corrosion Science* **165**, 2020 (108376).
60. A. Soleimani-Dorcheh and M. Galetz, *Oxidation of Metals* **84**, 2015 (73).
61. A. Solimani, T. Nguyen, J. Zhang, et al., *Corrosion Science* **176**, 2020 (109023).
62. A. Rahmel, M. Schütze, and W. Quadakkers, *Materials and Corrosion* **46**, 1995 (271).
63. I. Gurrappa and A. Gogia, *Materials Science and Technology* **17**, 2001 (581).
64. L. Mengis, C. Oskay, A. Donchev, et al., *Surface and Coatings Technology* **406**, 2021 (126646).
65. Institut für Arbeitsschutz DgU, Gestis-Stoffdatenbank (2023)
66. A. Navrotsky, *Physics and Chemistry of Minerals* **2**, 1977 (89).
67. A. Navrotsky, *Journal of the American Ceramic Society* **97**, 2014 (3349).
68. M. Lepple, K. Lilova, C. Levi, et al., *Journal of Materials Research* **34**, 2019 (3343).
69. G. Dbrowska, P. Tabero, and M. Kurzawa, *Journal of Phase Equilibria and Diffusion* **30**, 2009 (220).
70. K. Beck, T. König, E. Senvardarli, et al., *Materials and Corrosion* 2021 submitted
71. C. Giggins and F. Pettit, Hot corrosion degradation of metals and alloys - A unified theory. Pratt & Whitney Aircraft Group East Hartford, 1979
72. R. Rapp and K. Goto, *ECS Proceedings Volumes* **1**, 1981 (159).
73. S. Sunu, E. Prabhu, V. Jayaraman, et al., *Sensors and Actuators B: Chemical* **94**, 2003 (189).
74. R. Rathnasamy and V. Alagan, *Physica E: Low-Dimensional Systems and Nanostructures* **102**, 2018 (146).
75. M. Kassem, *Inorganic Materials* **42**, 2006 (165).

Authors and Affiliations

Katharina Beck[1] · Till König[1] · Ceyhun Oskay[1] · Andreas K. Czerny[2] · Frauke Hinrichs[3] · Georg Winkens[3] · Anke S. Ulrich[4] · Martin Heilmaier[3] · Mathias C. Galetz[1]

✉ Mathias C. Galetz
mathias.galetz@dechema.de

Katharina Beck
katharina.beck@dechema.de

Till König
till.koenig@dechema.de

Ceyhun Oskay
ceyhun.oskay@dechema.de

Andreas K. Czerny
andreas.czerny@kit.edu

Frauke Hinrichs
frauke.hinrichs@kit.edu

Georg Winkens
georg.winkens@kit.edu

Anke S. Ulrich
silvia.ulrich@uni-bayreuth.de

Martin Heilmaier
martin.heilmaier@kit.edu

[1] Materials and Corrosion, DECHEMA Research Institute, Theodor-Heuss-Allee 25, 60486 Frankfurt am Main, Germany

[2] Institute for Applied Materials-Applied Materials Physics, Karlsruhe Institute of Technology, Hermann-von-Helmholtz-Platz 1, 76344 Eggenstein-Leopoldshafen, Germany

[3] Institute for Applied Materials-Materials Science and Engineering, Karlsruhe Institute of Technology, Engelbert-Arnold-Straße 4, 76131 Karlsruhe, Germany

[4] Metals and Alloys II, University of Bayreuth, Prof.-Rüdiger-Bormann-Straße 1, 95447 Bayreuth, Germany